Asociación Argentina
de Mecánica Computacional

Mecánica Computacional Vol XXIX, págs. 3257-3279 (artículo completo)
Eduardo Dvorkin, Marcela Goldschmit, Mario Storti (Eds.)
Buenos Aires, Argentina, 15-18 Noviembre 2010

MASS-CONSERVING NUMERICAL SIMULATION OF PISTON RING/LINER CONTACT ALONG A FULL ENGINE CYCLE

Gustavo C. Buscaglia[a], Mohammed Jai[b], Jean-Paul Cadalen[c] and Franck Choukroun[c]

[a]*Inst. Ciências Matemáticas e de Computação, Univ. São Paulo, 13560-970 São Carlos, Brazil, gustavo.buscaglia@icmc.usp.br, http://www.lcad.icmc.usp.br/~buscaglia*

[b]*ICJ, INSA de Lyon (Pôle de Mathématiques), 69621 Villeurbanne, France, mohammed.jai@insa-lyon.fr, http://maths.insa-lyon.fr/~mjai*

[c]*RENAULT, 67, Rue des Bons Raisins, 92508 Rueil Malmaison, France, jean-paul.cadalen@renault.com, franck.choukroun@renault,com*

Keywords: Piston ring lubrication, cavitation, JFO conditions, engine.

Abstract. Of great concern for the automotive industry is the power lost to friction in the reciprocating components, in particular at the piston ring/liner contact. The piston rings seal the space between the piston and the liner, and act essentially as slider bearings subject to alternating motion. The numerical assessment of the ring/liner contact is very challenging due to the dynamical interaction of the oil film with the elastic rings, and the significant effect of cavitation and starvation phenomena. Important precedents can be found in the work of Priest and coworkers (e.g.; Proc. Inst. Mech. Engrs. 214:435-447, 2000).

In this article we report, to our knowledge for the first time, numerical simulations of the piston-ring assembly along a full engine cycle with a conservative formulation that is not restricted to one-dimensional configurations. We consider realistic applied loads on the rings, the actual crankshaft-connecting rod kinematics, and study both untextured and striated liners. It is shown that the rings' dynamics is strongly affected by starvation along the downwards strokes of the piston (intake, blow), leading to solid-solid contact of the compression ring. The effect of both transverse and oblique striations on this dynamics is assessed. The former induces an unstable behavior of the wiper ring, while the effect of the latter is more benign and indeed brings improvement at some parts of the cycle.

A brief discussion on the work that is still needed to accurately compute ring/liner lubrication is included as closure, with emphasis on the pitfalls of available mathematical models and on the numerical difficulties involved.

1 INTRODUCTION

Of great concern for the automotive industry is the power lost to friction in the reciprocating components, in particular at the piston ring/liner contact. The piston rings seal the space between the piston and the liner, and act essentially as slider bearings subject to alternating motion. Comprehensive theoretical modeling of piston ring lubrication has been undertaken by Priest (1996); Priest and Dowson (1999, 2000); Priest (2000).

Ongoing research aims at finding surface textures that minimize the friction losses at the ring/liner contact. This is certainly related to the more fundamental question of whether the friction of a slider bearing can be reduced by texturing the surface. Pin-on-disk and other experimental tests have been conducted in several studies (see, e.g., Uehara et al. (2004); Wakuda et al. (2003); Yagi et al. (2008); Yu et al. (2010); Zum Gahr et al. (2007), of which some have given evidence of friction reduction, mainly in the mixed lubrication regime. On the theoretical side, some authors have modeled the problem using the Reynolds' boundary condition at the cavitation boundaries. This boundary condition does not conserve mass, and though in some cases it provides acceptable accuracy, it fails miserably in many cases of interest, in particular when the surfaces are textured. This was first pointed out by Ausas et al. (2009b), and more recently further elaborated upon by Qiu and Khonsari (2009)

The assessment of the hydrodynamics of ring/liner contact thus requires physically sound numerical models. In principle, the (multifluid) Navier-Stokes equations with free surfaces should be solved, but this is far beyond current capabilities. Always keeping in mind its limitations (Dobrica and Fillon, 2008), the Reynolds-equation-based model with Jacobson-Floberg-Olsson boundary conditions, in the formulation introduced by Elrod and Adams (Elrod-Adams model hereafter), is the best available candidate. Piston ring simulations based on the Elrod-Adams model with moving textures in the dynamical case have not yet been reported in the literature. Our purpose here is to adapt the algorithm proposed by Ausas et al. (2009a) to the piston ring case, and perform simulations under conditions corresponding to an automotive engine at 2000 rpm.

2 MODELING

2.1 Geometrical model

We consider the configuration shown in Fig. 1. Three rings are in contact with the liner, namely the compression ring (ring 1), the wiper ring (ring 2) and the oil ring (ring 3). The surface of the liner is developed along the $x_1 - x_2$ plane, x_1 being the axial direction (coincident with that of the piston motion) and x_2 the circumferential one. The curvature along x_2 is neglected, in view of the large ratio between the circumference length and the piston/liner gap thickness.

It is assumed that the rings are only allowed to move along x_3, their positions being parameterized by Z_1, Z_2 and Z_3, respectively. The origin of the Z_i's is chosen so that $Z_i = 0$ corresponds to the ring i touching the $x_1 - x_2$ plane.

Each ring has some given profile, $h_i(x_1, x_2)$ ($i = 1, 2, 3$), which as a result of the definition of the Z_i's satisfy $\min_{(x_1,x_2)} h_i(x_1, x_2) = 0$. The actual profiles considered here are shown in Fig. 2.

The liner is assumed to coincide with the $x_1 - x_2$ plane ($x_3 = 0$) when it is smooth (untextured). In the textured case, it is given by some function $x_3 = -h_L(x_1, x_2) \leq 0$. We consider here texture patterns inspired from striated surfaces which are frequently found in liners. They are idealized as parallel striations of depth δ and width ξ, which repeat periodically with period

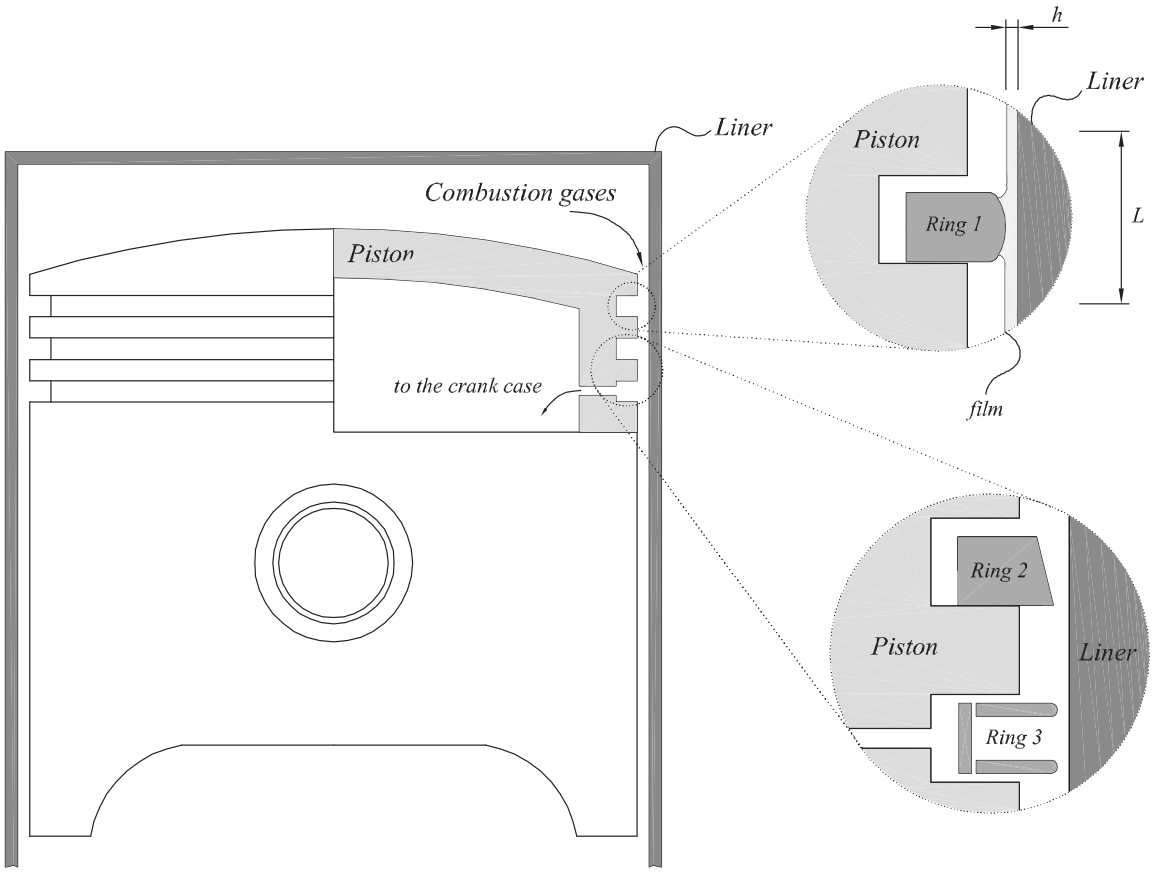

Figure 1: Scheme of the piston/cylinder system.

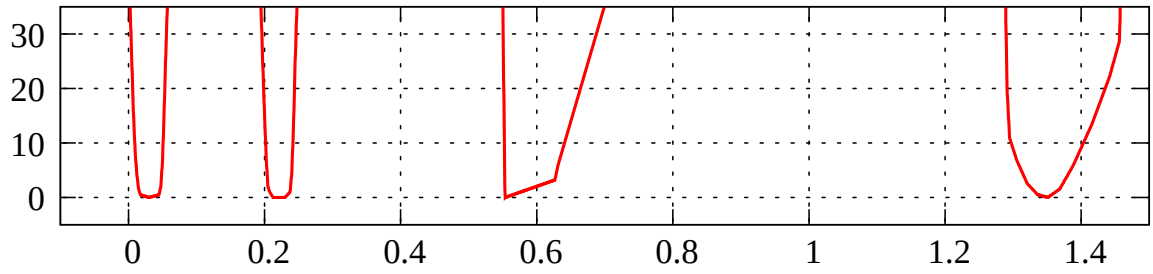

Figure 2: Profiles of the rings.

λ. These striations form an angle γ with the direction of motion x_1. This is the case that will be denoted hereafter as "simply striated". The second case consists of combining two equivalent simple striations, of the same characteristics, at angles $+\gamma$ and $-\gamma$. It will be denoted as "cross striated". In any of the cases, the problem becomes periodic in x_2, so that in the simulation only one period is considered, $0 < x_2 < B$, with suitable boundary conditions at $x_2 = 0$ and $x_2 = B$.

The piston follows a motion given by $x_1 = \phi(t)$, corresponding to the classical crankshaft-connecting rod mechanism. Assuming inertial forces along x_1 to be negligible, we adopt a frame of reference that moves with the piston. The rings then occupy fixed regions of the $x_1 - x_2$ plane, that we denote by I_i, and that in fact are bands parallel to the x_2 axis. More specifically, ring number i occupies the region $a_i < x_1 < b_i$. Outside of the rings' positions the gap between piston and liner is assumed uniform of thickness e (notice that this implies, in particular, that the piston is centered and aligned with the cylinder, which constitutes of course an idealization).

Under the assumptions above, the gap between the piston-ring assembly and the liner is given by

$$h(x_1, x_2, t) = \begin{cases} h_L(x_1 - \phi(t), x_2) + h_i(x_1, x_2) + Z_i(t) & \text{if } a_i < x_1 < b_i \\ h_L(x_1 - \phi(t), x_2) + e & \text{otherwise} \end{cases} \tag{1}$$

The piston displacement $\phi(t)$ that we consider here, together with the relative velocity between piston and cylinder $u(t)$ (which due to our choice of reference frame equals $-\phi'(t)$ are depicted in Fig. 3 *as functions of the crank angle* $\zeta = \omega t$, where ω stands for the angular frequency (in rad/s for example) of the crank.

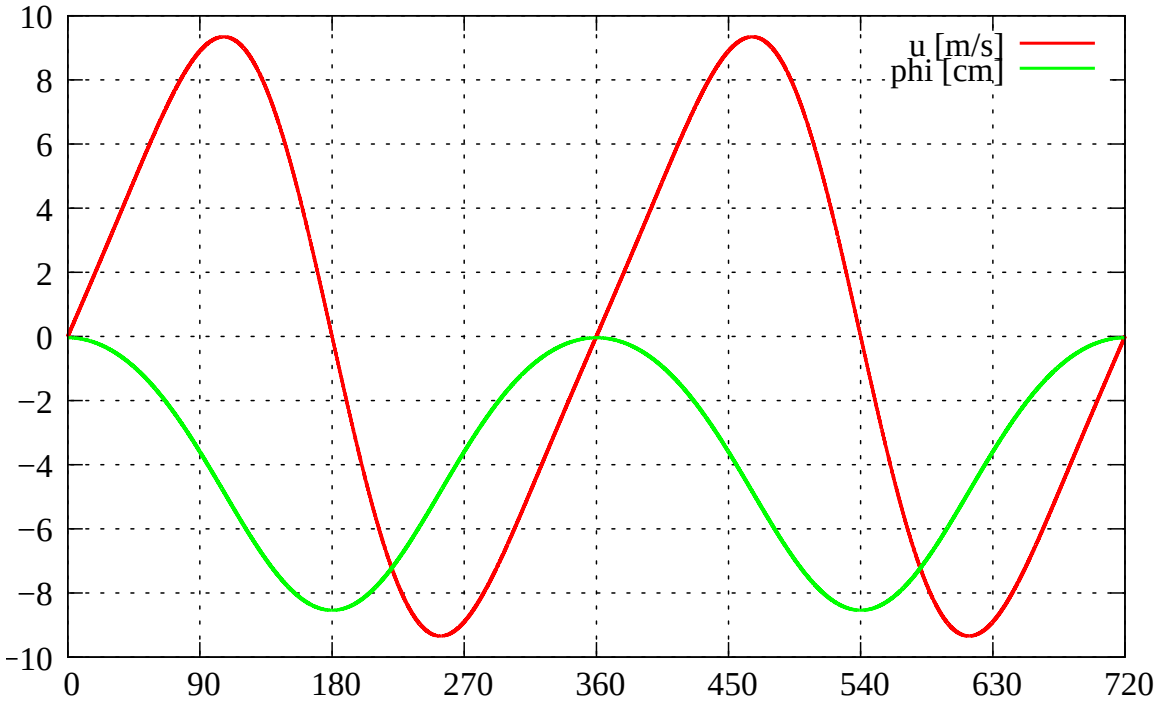

Figure 3: Displacement of the piston and relative velocity.

2.2 Forces on the rings

The dynamics of the rings is governed by the forces acting on them along the x_3-direction. These forces are originated on four different physical mechanisms, as described below.

The *pre-stress force* comes from the elastic response of the ring to the deformation needed to make it fit into its placement. It points outwards (i.e.; along $-x_3$) and can be assumed constant. We denote by W_i^{ps} its value *per unit length along* x_2. The values adopted here are $W_1^{ps} = -325$ N/m, $W_2^{ps} = -290$ N/m and $W_3^{ps} = -704$ N/m.

The *gas-pressure force* originates from the leakage of cylinder pressure through the narrow gaps that exist between the rings and the piston. It mainly affects ring 1 (compression ring) but also has some effect on ring 2 (wiper ring). This is a time-dependent force for which we adopt the values (*per unit length along* x_2)

$$W_1^{gp}(t) = -0.9 \times 10^{-3}\text{m} \times p_c(t), \qquad W_2^{gp}(t) = -0.5 \times 10^{-4}\text{m} \times p_c(t), \qquad W_3^{gp}(t) = 0$$

where the cylinder pressure $p_c(t)$ is shown, as a function of the crank angle, in Fig. 4.

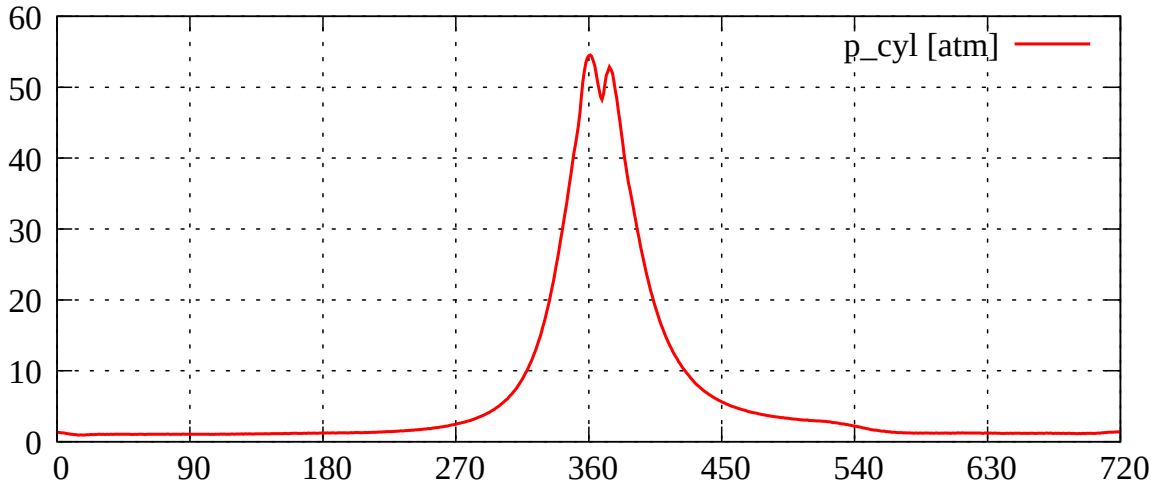

Figure 4: Pressure in the cylinder as a function of the crank angle.

The *hydrodynamic force* originates from the pressure $p(x_1, x_2, t)$ that develops in the oil film between the ring and the liner. Its value per unit length along x_2 is given by

$$W_i^h(t) = \frac{1}{B} \int_{a_i}^{b_i} \int_0^B p(x_1, x_2, t)\, dx_1\, dx_2 \tag{2}$$

The pressure field p comes out from the hydrodynamic model that is described in the next subsection.

The *contact force* originates from the direct contact between the asperities of the surfaces. It is given by

$$W_i^c(t) = \frac{1}{B} \int_{a_i}^{b_i} \int_0^B p_{\text{con}}(x_1, x_2, t)\, dx_1\, dx_2 \tag{3}$$

For the contact pressure p_{con} we adopt the Greenwood-Williamson model (Greenwood and Williamson, 1966), more specifically the expression provided by Panayi and Schock (2008).

The contact pressure is thus calculated as

$$p_{\text{con}} = \begin{cases} E^* C_7 \left[C_6 + \exp\left(\frac{C_1 + C_2 \frac{h}{\sigma} + C_3 \frac{h^2}{\sigma^2}}{1 + C_4 \frac{h}{\sigma} + C_5 \frac{h^2}{\sigma^2}} \right) \right] & \text{if } h < 4\sigma \\ 0 & \text{otherwise} \end{cases} \tag{4}$$

where E^* is the combined Young modulus of the two surfaces, σ is the composite rms amplitude of the roughness ($\sigma = \sqrt{\sigma_1^2 + \sigma_2^2}$), and the constants take the values $C_1 = -0.48347$, $C_2 = -1.65118$, $C_3 = 0.06043$, $C_4 = -0.19256$, $C_5 = 0.01610$, $C_6 = -3.50796 \times 10^{-6}$ and

$$C_7 = \frac{16\sqrt{2}}{15} \pi (\eta \beta \sigma)^2 \sqrt{\frac{\sigma}{\beta}}$$

with η the asperity density and β the asperity radius of curvature. In the cases we consider $C_7 = 0.64892$, $E^* = 10^{11}$ Pa and $\sigma = 0.14$ microns.

From the above considerations, if m_i is the mass of ring $\#i$ per unit length, then the dynamical equations for the rings' displacements read

$$m_i \frac{d^2 Z_i}{dt^2} = W_i^{ps}(t) + W_i^{gp}(t) + W_i^{h}(t) + W_i^{c}(t) \tag{5}$$

for $i = 1$, 2 and 3. This is supplemented with initial conditions for Z_i and Z_i' at $t = 0$. For the model to be in closed form it only remains to explain the calculation of the hydrodynamic pressure p.

2.3 Hydrodynamics and cavitation modeling

We adopt here the well-known Elrod-Adams model (Elrod and Adams, 1974), which incorporates into a single formulation Reynolds equation for the pressurized region and Jacobsson-Floberg-Olsson boundary conditions. This model is mass conserving, which as shown by Ausas et al. (2009b) is essential for obtaining physically meaningful results in lubrication problems involving textured surfaces.

The model postulates the computation of two fields, p and θ, which correspond to the hydrodynamic pressure and an auxiliary saturation-like variable, respectively, which (weakly) satisfy the equation

$$\nabla \cdot \left(\frac{h^3}{12\mu} \nabla p \right) = \frac{u(t)}{2} \frac{\partial\, h\theta}{\partial x_1} + \frac{\partial\, h\theta}{\partial t} \tag{6}$$

under the complementarity conditions

$$\begin{cases} p > 0 & \Rightarrow & \theta = 1 \\ \theta < 1 & \Rightarrow & p = 0 \\ 0 \le \theta \le 1 & & \end{cases} \tag{7}$$

where μ is the viscosity of oil.

This model has been analyzed to great extent by Bayada and Chambat (1986); Bayada et al. (1990), and it has been shown that leads to well-posed problems in several physically-meaningful situations. For the piston ring/liner contact we assume that the oil-film thickness is known (and constant, equal to d_{oil}) far away from the ring assembly. This amounts to imposing that $\theta = d_{\text{oil}}/h$ at the boundary of the computational domain. More precisely, if the computational domain corresponds to $x_{1\ell} < x_1 < x_{1r}$, then when $u(t) > 0$ we impose

$\theta(x_{1\ell}, x_2, t) = d_{\text{oil}}/h(x_{1\ell}, x_2, t)$ and when $u(t) < 0$ we impose $\theta(x_{1r}, x_2, t) = d_{\text{oil}}/h(x_{1r}, x_2, t)$. For brevity, we denote

$$x_1^-(t) = \begin{cases} x_{1\ell} & \text{if } u(t) > 0 \\ x_{1r} & \text{if } u(t) < 0 \end{cases} \tag{8}$$

As already said, the boundary conditions along $x_2 = 0$ and $x_2 = B$ are defined so as to enforce the proper periodicity in that direction. An initial condition for θ is also provided.

As a consequence of the previous model, at each instant the domain spontaneously divides into a pressurized region, Ω^+, where $p > 0$, and a cavitated region, Ω^0, where the film is not full ($\theta < 1$). At the boundary between Ω^+ and Ω^0, the so-called cavitation boundary Σ, the Elrod-Adams model automatically enforces the mass-conservation condition

$$\frac{h^3}{12\mu}\,\nabla p \cdot \hat{n} = \frac{u(t)}{2}(1-\theta)\; h\, \hat{n} \cdot \hat{i} \tag{9}$$

where $\hat{n}$ is the normal to Σ (oriented outwards from Ω^0) and $\hat{i}$ is the unit vector along x_1. In particular, the saturation field θ turns out to be discontinuous at those parts of Σ where $u(t)\hat{n} \cdot \hat{i}$ is positive (reformation boundary).

If the gap thickness h is discontinuous at the cavitation boundary, which is often the case in the textured case, Eq. 9 does not hold. However, the Elrod-Adams model considered as a conservation law $\partial_t \varphi + \nabla \cdot J = 0$, with $\varphi = h\,\theta$, remains in general well-posed and provides a physically-meaningful solution (the theory is somewhat fragmented and does not cover all possible conditions, but sufficient evidence exists to safely assume well-posedness under initial and boundary conditions that make physical sense).

2.4 Friction losses

The friction force per unit width is given by

$$F_i = \frac{1}{B}\int_{a_i}^{b_i}\int_0^B \left(\frac{\mu u(t) g(\theta)}{h} + 3h\frac{\partial p}{\partial x_1} + \mu_S\, p_{\text{con}}\right)\, dx_1\, dx_2 \tag{10}$$

where the function $g(\theta)$ is taken either as a switch function ($g(\theta) = 1$ if $\theta = 1$, otherwise $g = 0$) that neglects any friction in the cavitation region, or as a continuous function that accounts for streamers ($g(\theta) = \theta$). We denote by $F_{st,i}$ the friction force computed with the streamers version of g.

The friction coefficient then results from

$$f_i = \frac{F_i}{W_i^{ps} + W_i^{gp}} \tag{11}$$

2.5 Adimensionalization and final equations

We consider an adimensionalization of the equations based on the following fundamental scales:

Quantity	Scale	Adopted value
Velocity	U	10 m/s
Length	L	1 cm
Gap thickness	H	1 μm

These scales, together with the viscosity of the oil, assumed to be $\mu = 0.004$Pa-s lead to the following derived scales for the different quantities

Quantity	Scale	Adopted value	Name
x_1, x_2	L	10^{-2} m	
t	$\frac{L}{U}$	10^{-3} s	time
h	H	10^{-6} m	gap thickness
Z_i	H	10^{-6} m	ring's radial position
p, p_{con}	$\frac{6\mu UL}{H^2}$	2.4×10^9 Pa	pressure
$W_i^{ps}, W_i^{gp}, W_i^h, W_i^c$	$\frac{6\mu UL^2}{H^2}$	2.4×10^7 N/m	radial forces per unit width
F_i	$\frac{\mu UL}{H}$	4×10^2 N/m	friction forces per unit width
m_i	$\frac{6L^4\mu}{H^3U}$	2.4×10^7 kg/m	mass per unit width

Notice that, since the scales for radial and friction forces are different, the friction coefficient is given by

$$f_i = \frac{H}{6L}\,\frac{\hat{F}_i}{\hat{W}_i^{ps} + \hat{W}_i^{gp}} \tag{12}$$

where the carets (hats) denote the corresponding non-dimensional quantity.

Upon adimensionalization of all variables, and omitting all carets for simplicity, let us collect the complete mathematical problem to be solved:

"Find trajectories $Z_i(t)$ ($i = 1, 2, 3$), and fields $p(t)$, $\theta(t)$, defined on $\Omega = (x_{1\ell}, x_{1r}) \times (0, B)$ and periodic in x_2, satisfying

$$\left\{\begin{array}{l} Z_i(0) \;=\; Z_{i0}, \qquad Z_i'(0) \;=\; V_{i0}, \qquad i = 1,2,3 \\ \theta(x_1^-(t), x_2, t) = d_{\text{oil}}/h(x_1^-(t), x_2, t) \qquad \forall x_2 \;\in\; (0, B) \\ p \;>\; 0 \qquad \Rightarrow \qquad \theta \;=\; 1 \\ \theta \;<\; 1 \qquad \Rightarrow \qquad p \;=\; 0 \\ 0 \;\leq\; \theta \;\leq\; 1 \end{array}\right. \tag{13}$$

and

$$m_i \frac{d^2 Z_i}{dt^2} \;=\; W_i^{ps}(t) + W_i^{gp}(t) + W_i^h(t) + W_i^c(t) \tag{14}$$

$$\nabla \cdot \left(h^3 \nabla p\right) \;=\; \frac{u(t)}{2}\,\frac{\partial\, h\theta}{\partial x_1} + \frac{\partial\, h\theta}{\partial t} \tag{15}$$

where

$$h(x_1, x_2, t) \;=\; \left\{\begin{array}{ll} h_L(x_1 - \phi(t), x_2) + h_i(x_1, x_2) + Z_i(t) & \text{if } \; a_i < x_1 < b_i \\ h_L(x_1 - \phi(t), x_2) + e & \text{otherwise} \end{array}\right. , \tag{16}$$

$$W_i^h(t) \;=\; \frac{1}{B}\int_{a_i}^{b_i}\int_0^B p(x_1, x_2, t)\; dx_1\; dx_2\;, \tag{17}$$

$$W_i^c(t) \;=\; \frac{1}{B}\int_{a_i}^{b_i}\int_0^B p_{\text{con}}(x_1, x_2, t)\; dx_1\; dx_2\;, \tag{18}$$

the functions $u(t)$, $W_i^{ps}(t)$, $W_i^{gp}(t)$, $\phi(t)$, $h_L(x_1, x_2)$, $h_i(x_1, x_2)$ are known explicitly, and p_{con} is a given function of h."

2.6 Numerics

The numerical treatment is exactly that described in Ausas et al. (2009a). It consists of a finite volume, conservative method with upwinding discretization of the Couette flux and centered discretization of the Poiseuille flux and an iterative imposition of the cavitation conditions ($p \geq 0$; $\theta < 1 \Rightarrow p = 0$; $p > 0 \Rightarrow \theta = 1$) by means of a Gauss-Seidel-type algorithm. The dynamical equation for $Z(t)$ is discretized by a Newmark scheme, which is built into the overall iterative process.

3 NUMERICAL SIMULATIONS AT 2000 RPM

3.1 Untextured liner

The code was run at 2000 rpm, corresponding to a relation between crank angle and time of $\zeta(t) = 12t + \zeta_0$, where ζ is in degrees, t is non-dimensional, and ζ_0 was chosen as 210 degrees. This corresponds to a non-dimensional time of 60 for one 720-degree cycle of the piston. The simulation time was 200 units, and a periodic behavior was attained already at the third cycle. The simulation domain was taken as $-0.577 < x_1 < 1.732$, with about half a centimeter separating the ring pack from the left and right boundaries. The initial film thickness, together with the thickness of oil at inflows, was taken as 5 microns.

The time and space discretization steps were chosen as $\Delta t = 1.25 \times 10^{-3}$ (48000 time steps per engine cycle) and $\Delta x = 3.61 \times 10^{-3}$ (640 divisions in x_1).

3.1.1 Movement of the rings

In Fig. 5 we plot a cycle, between $t = 102.5$ (crank angle of zero degrees) and $t = 162.5$ (crank angle of 720 degrees), beginning with the piston at the top dead center just before intake. Notice that a positive velocity corresponds to the piston going downwards.

The first phenomenon to be observed is, at time ~ 108.5 (corresponding to a crank angle of 72 degrees), that the gap between ring 1 and the liner falls from 2.1 microns to 0.43 microns (which corresponds to solid-solid contact). The reason for this can be inferred from the solutions between time 102.5 and 109 shown in Fig. 6. In those graphs, as in those that are shown later, the oil thickness (equal to $\theta\, h$) has been designed as lying on the liner just to ease the interpretation. This is certainly true at the *inflows*, since the flow there is simply the amount of oil present on the liner in relative movement with respect to the piston, but is just an idealization once the oil has passed under any of the rings.

Coming back to Fig. 6, we observe that the compression ring (ring 1, the rightmost in the figure) starts its descent (suction stroke) by lifting under the action of increasing velocity and sufficient oil supply accumulated on top (to the right in the figure) of the wiper ring in its way up. However, the wiping action of ring 2 is much more efficient on its way down, and at time ~ 108.5 the compression ring goes into starvation and comes into direct contact with the liner. Ring 2 is in contact all along the descent, while Ring 3 detaches just a little bit (about half a micron).

At time 117.5 the piston is at its bottom dead center, and then its starts moving upwards (meaning that the liner starts moving to the left in the figures). The evolution of the system along this part of the cycle (compression stroke) is shown in Fig. 7. Remember that at the boundaries the oil thickness is assumed to be of 5 microns. In this stroke this boundary condition could be questionable, since it assumes that there exists some oil source that replenishes the liner layer after the rings have passed. Any way, this assumed fresh layer of oil arriving from the right gets

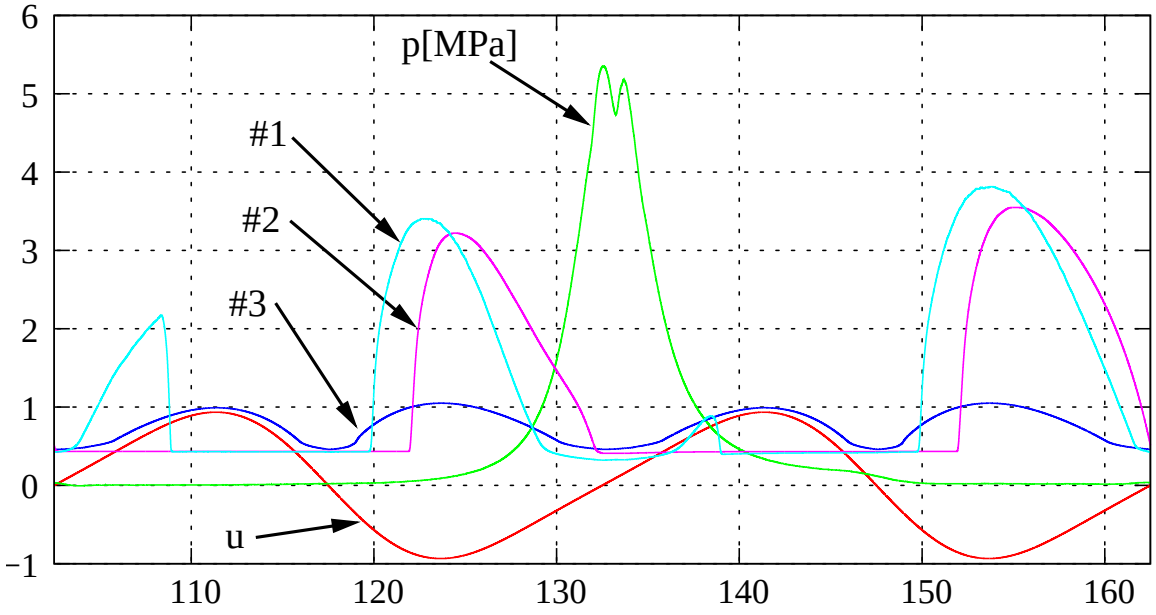

Figure 5: Piston velocity (non-dimensional) and cylinder pressure (in MPa) for an engine cycle as functions of non-dimensional time, together with the radial positions $Z_i(t)$ of the three rings (in microns).

to Ring 1 at $t \simeq 120$, allowing it to lift by hydrodynamic action, and the same happens with Ring 2 at $t \simeq 122$. Notice how the much better hydrodynamical behavior of Ring 2 in upwards motion is captured by the simulation. By $t \simeq 130$ Ring 1 eventually comes back into contact with the liner as a consequence of increased cylinder pressure loading and diminishing velocity, and the same happens with Ring 2 at $t \simeq 132$, which is close the pressure peak and to the top dead center.

Along the second downwards motion of the piston (the power stroke) the physical picture of the ring/liner contact is pretty much the same as along the suction stroke, except that Ring 1 detaches less from the liner before it gets starved (which happens at about the same angle, at $t \simeq 138.5$, crank angle of 432 degrees). The behavior along the second upwards motion, going from time 147.5 to 162.5 (blow stroke), also resembles closely what happens at the compression stroke. Some instants can be seen in Fig. 8.

3.1.2 Friction

The time evolution of the friction forces and of the friction power losses (product of force times velocity) is depicted in Figs. 9 and 12, along a cycle (to simplify the analysis we turn to plot in terms of the crank angle instead of time).

The largest friction forces take place near the top dead center at ignition, and are logically most severe for Ring 1, which is pushed against the liner by the cylinder pressure. Dividing at each instant the friction force by the applied load (pre-stress plus gas-pressure forces) it is possible to obtain the instantaneous apparent friction coefficient, which is shown in Fig. 10. The observed values should be understood in terms of the Stribeck parameters observed along the cycle, for which we define an instantaneous value by

$$St(t) := \frac{\mu u(t)}{W^{ps} + W^{gp}(t)} \tag{19}$$

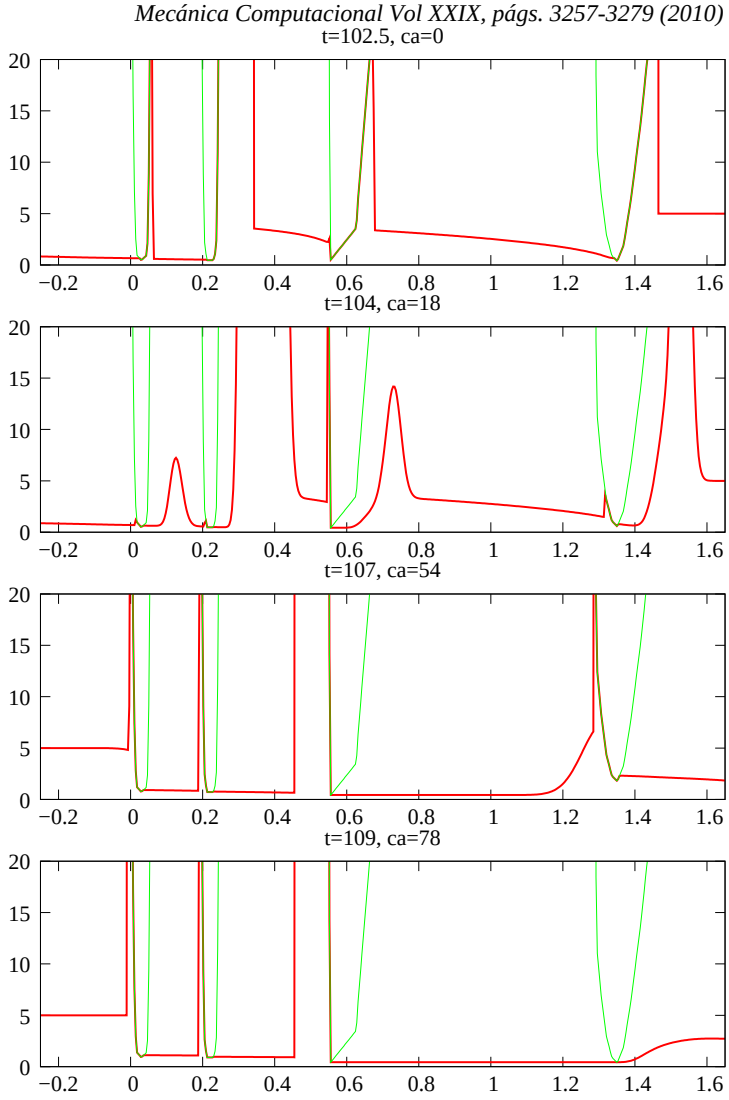

Figure 6: Oil thickness profiles (suction stroke).

and we plot it in Fig. 11. We observe that along most of the cycle St is above 10^{-5} for all rings, which for full-film conditions lead (according to previous results) to hydrodynamic or mixed conditions on the three rings. However, Fig. 10 shows that rings 1 and 2 exhibit friction coefficients corresponding to solid-solid contact along most of the suction and power strokes. This is due to starvation of these rings, as already discussed.

Of more practical importance is the power loss, which also shows evidence of this behavior. The contributions to power loss of the three rings are comparable, most of the time the largest one corresponding to Ring 1 (see Fig. 12), followed by Ring 2. Power loss is again significant around ignition, but it is also very important during the suction stroke and during the end of the power stroke. This is because in these downwards movements the wiper ring is in solid contact with the liner, and as discussed before the compression ring becomes starved at about 72 degrees from the top dead center and also becomes in solid contact with the liner. Overall, the average non-dimensional friction power equals 0.1105, with 0.0498 (45%) for Ring 1, 0.0342 (31%) for Ring 2 and 0.0265 (24%) for Ring 3.

The power loss can also be decomposed between hydrodynamic loss (power dissipated due to hydrodynamic friction) and solid-contact loss (power dissipated due to solid contact). This

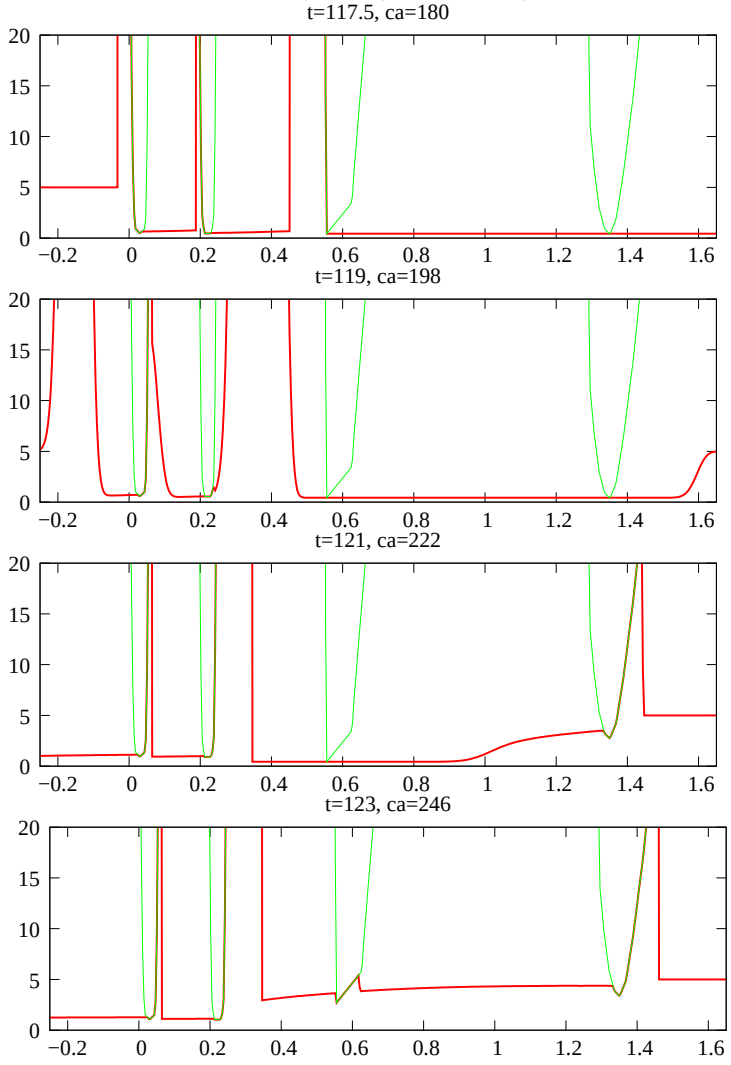

Figure 7: Oil thickness profiles (compression stroke).

is shown in Fig. 13.

In fact, the average power dissipated hydrodynamically along the cycle is 0.038 (34%), while that dissipated by solid contact is 0.072 (66%).

3.2 Transversely textured liner

A simulation was performed with a transversely textured liner, in which the texture only depends on x_1, periodic with period λ and depth δ. The specific shape is given by (see also Fig. 14.

$$h_L(x_1,x_2) = \begin{cases} 0 & \text{if } x_1 < \frac{\lambda}{2} \\ \delta\left(\frac{4x_1}{\lambda} - 2\right) & \text{if } \frac{\lambda}{2} x_1 < \frac{3\lambda}{4} \\ \delta\left(4 - \frac{4x_1}{\lambda}\right) & \text{if } \frac{3\lambda}{4} x_1 < \lambda \end{cases}$$

We took $\lambda = 0.5$ mm and $\delta = 0.5$ microns (for larger depths the wiper ring became unstable). The rest of the conditions are as in the untextured case (including the mesh and time step). In Fig. 15 we show the minimum distance between each ring and the liner as functions of time. Notice that due to the presence of texture, the minimum distance does not coincide with the radial position of the ring (Z_i), which is shown in Fig. 16. These are highly oscillatory

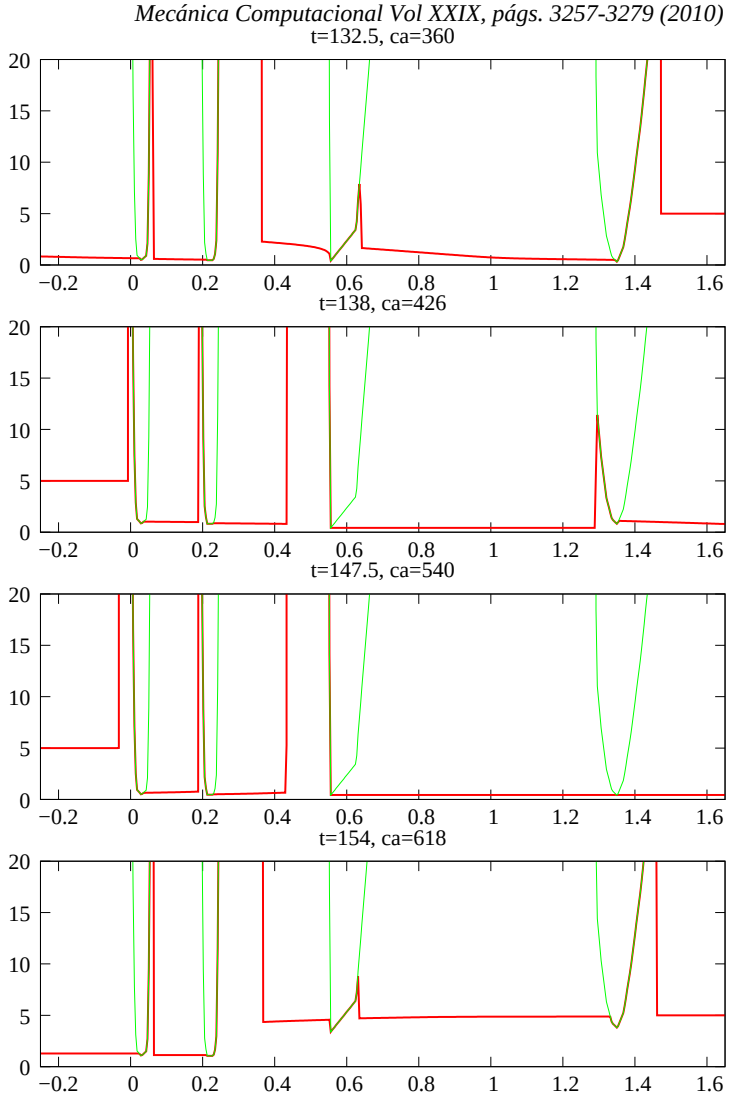

Figure 8: Oil thickness profiles (blow stroke).

quantities due to the passage of the textures under the rings, and thus hard to analyze. The same happens with the friction power, shown in log scale in Fig. 17. Notwithstanding, the *average* friction power turns out to be strikingly low, of 0.0778 (30 % smaller than for the untextured liner!), decomposed into 0.0255 for Ring 1, 0.0257 for Ring 2 and 0.0266 for Ring 3. Also, of the total power loss 0.0397 corresponds to hydrodynamic dissipation and 0.0381 to solid-contact dissipation. It is thus observed that the main reductions in friction have taken place in Rings 1 and 2, and that they have affected mainly the solid-contact dissipation.

To further understand the impact of the texture we then process the friction power data, averaging each point over 161 time steps (80 on each side). Since the total friction loss is the integral of the friction power, and the time step is constant, this filtering does not affect the quantities of interest but allows us to get a picture of the phenomena that are taking place. We compare the filtered friction power with that of the untextured case in Fig. 18, while in Figs. 19 and 20 we show the same comparisons for the compression and wiper rings, respectively.

Figure 18 is very useful in the sense that it clearly shows where along the cycle the transverse texture reduces friction. The most important reduction takes place along the suction and power strokes.

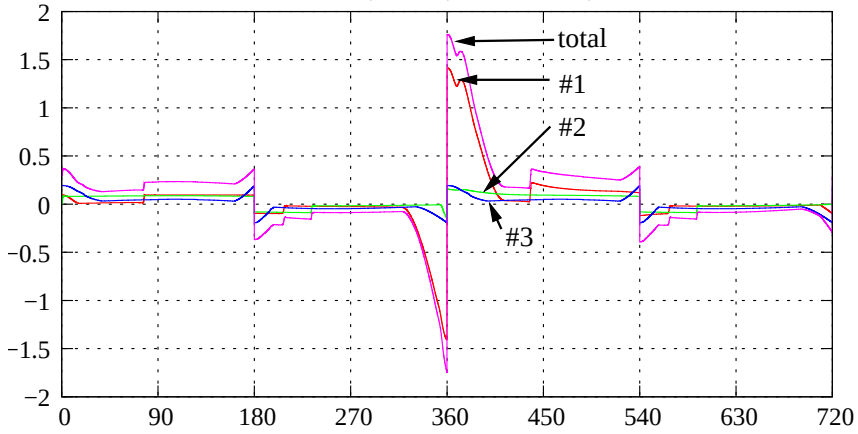

Figure 9: Non-dimensional friction force as a function of the crank angle

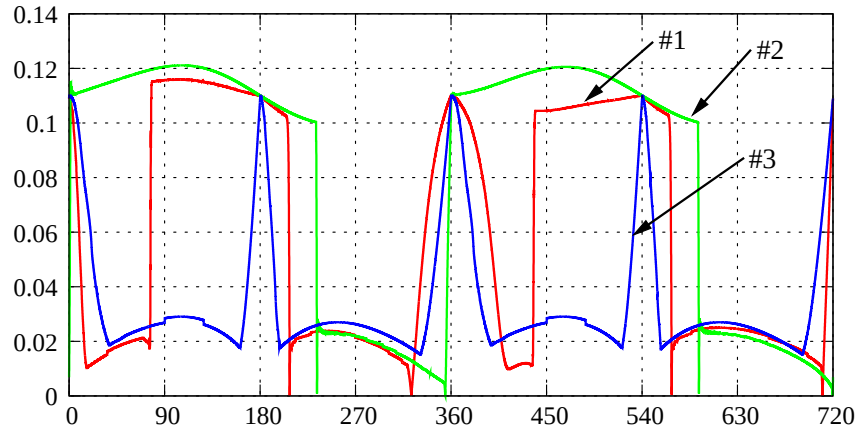

Figure 10: Instantaneous apparent friction coefficient as a function of the crank angle

For the compression ring, the main difference is that the texture avoids the sudden increases in friction that arise at crank angles of 72 and 432 degrees. Apparently, the compression ring remains at a larger distance from the liner simply because the oil thickness arriving to it from the wiper is 1 micron, instead of the 0.4 microns that arrived to it in the untextured case and led it to solid contact. The compression ring accompanies the passage of the texture without any striking phenomenon taking place. We thus turn our attention to the wiper ring.

A sequence of images of the oil film near the wiper ring at crank angles near 90 degrees can be observed in Figs. 21 and 22. By inspection, it is seen that the wiper exhibits a rather chaotic, non-periodic movement, which leads to excursions of up to 2 or more microns away from the liner (e.g.; see angle 90.3). These oscillations also take it very close to the liner, as at crank angle 91.05. The net effect of these excursions is that a thicker oil film passes under the wiper ring than in the untextured case (see bottom graph in Fig. 22).

Notice also that the behavior of the oil ring does not change much from the untextured to the textured case. We see an oil thickness of about 1 micron left by the oil ring arriving to the wiper ring in both cases. It is thus concluded that the oscillatory behavior of the wiper ring, leaving behind it a thicker oil film and inhibiting starvation of the compression ring, is responsible for the lower friction losses shown by the textured liner in the simulations.

We remark firstly that though friction losses are diminished, the strong oscillations of the

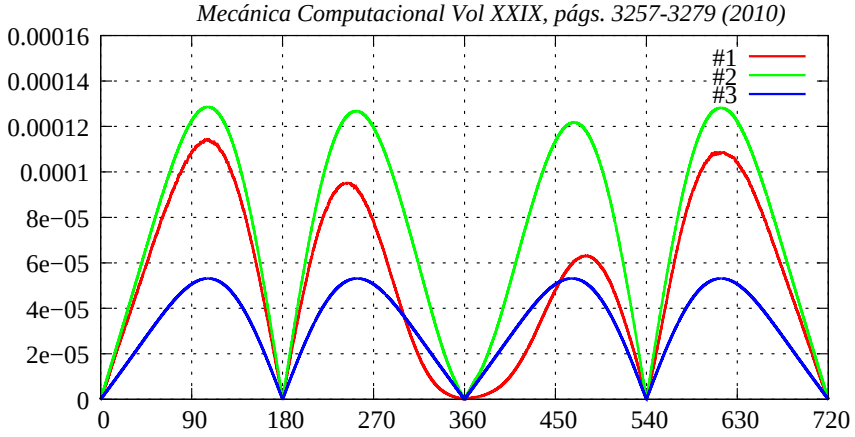

Figure 11: Instantaneous Stribeck parameter as a function of the crank angle

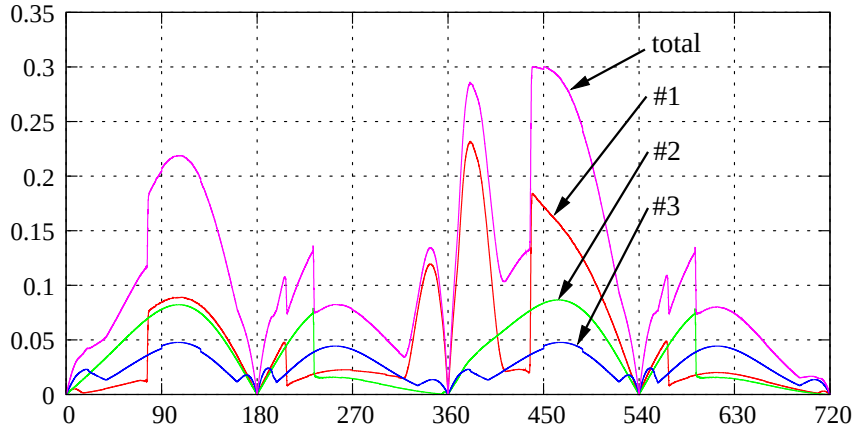

Figure 12: Non-dimensional friction power loss as a function of the crank angle

wiper ring would probably lead to fatigue and failure. Also, such an oscillatory behavior challenges the resolution and modeling capabilities of the numerical scheme. To check that the phenomena described above are not mere numerical artifacts, another simulation of the transversely textured bearing was run with twice the number of cells and of time steps. Though there is an effect of the mesh and time step, the qualitative behavior seems to be independent of numerical error. It is clear that the average position is much more distant from the liner than in the untextured case

The friction reduction predicted for the transversely textured liner thus results from oscillations of the wiper ring, which in turn arise from the ring following the profile of the texture to some extent. This can only happen if the striations are exactly aligned with the ring, which is unlikely. To further investigate the effect of striations in unaligned cases, simulations were run with cross-striations, which are described in the next section.

3.3 Cross-striated liner

A simulation was performed under the same conditions as before, with a cross-striated liner of angle $\gamma = 60$ degrees, width $\xi = 0.125$ mm and period $\lambda = 0.5$ mm. The striation bottom is planar, that is, inside the striations the depth is constant, of 5 microns.

To compare with the transversely-striated case, we begin by plotting the distance of each

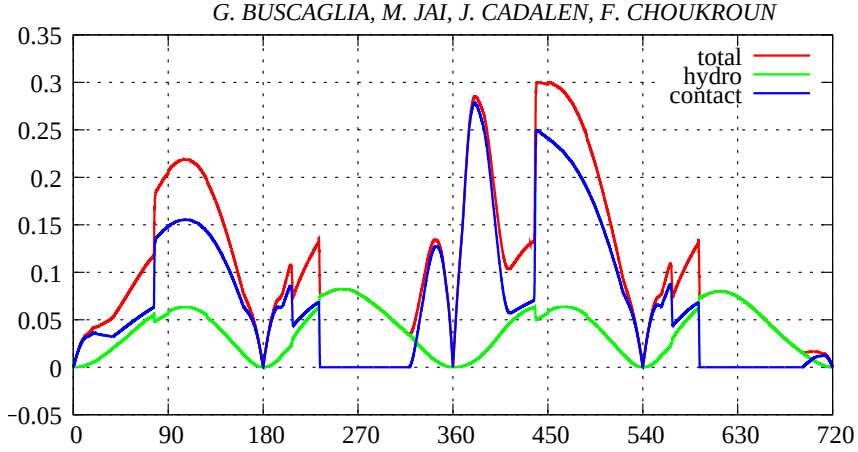

Figure 13: Non-dimensional friction power loss as a function of the crank angle, decomposed into hydrodynamic and solid-contact components.

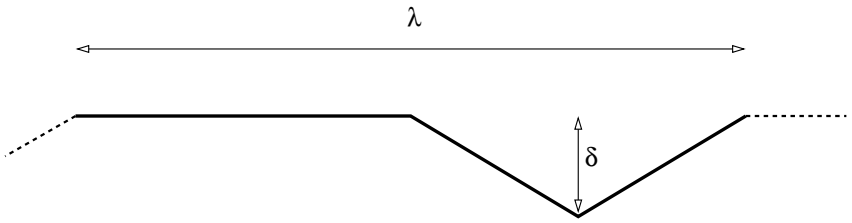

Figure 14: Scheme of the transverse texture.

ring to the liner in Fig. 23. Notice the big differences with the untextured case (Fig. 5). All the rings are now much closer to the liner, and the detachments of rings 1 and 2 during the upwards strokes are of less than 1 micron. The friction power along the cycle is shown in Fig. 24. The behavior is quite different from that in the untextured case. Along the suction stroke, the compression ring dissipates very little power, since it does not become starved. This makes that along the suction stroke, and also along the second half of the power stroke, the cross-striated liner turns out to be convenient with respect to the untextured ones in terms of friction, according to these simulations. On the other hand, the friction power near 360 degrees is quite higher than that for the untextured liner. Also, the oil ring along the whole cycle dissipates more power. Overall, the average friction power dissipated is 0.1218 (10 % higher than for the untextured liner), decomposed as 0.0415 for Ring 1, 0.0322 for Ring 2 and 0.0482 for Ring 3.

3.3.1 Effect of the rings' masses

The behavior of the system is strongly governed by the dynamics of the rings. As an example, we show in Fig. 25 the effect of multiplying the masses of the rings by a factor of 10. A significant reduction in the losses is observed, which comes from the detachment of the wiper ring from the liner along the downward strokes (shown for the suction stroke in Fig. 26. This is a phenomenon similar to that observed for the transversely textured liner, and causes more oil to be left behind by the wiper, inhibiting starvation of the compression ring but also increasing the oil consumption. A preliminary computation with the true masses (ten times smaller than in the original simulations), on the other hand, yielded little difference with the reported results.

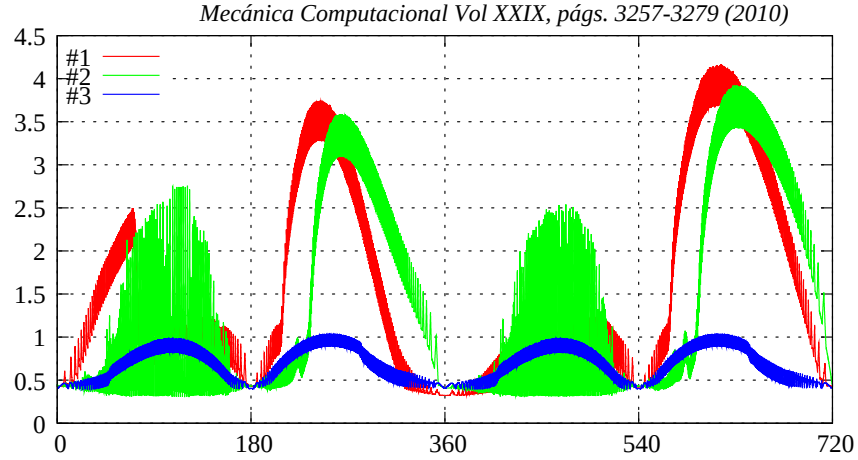

Figure 15: Minimum distance between each ring and the liner, for the transverse texture.

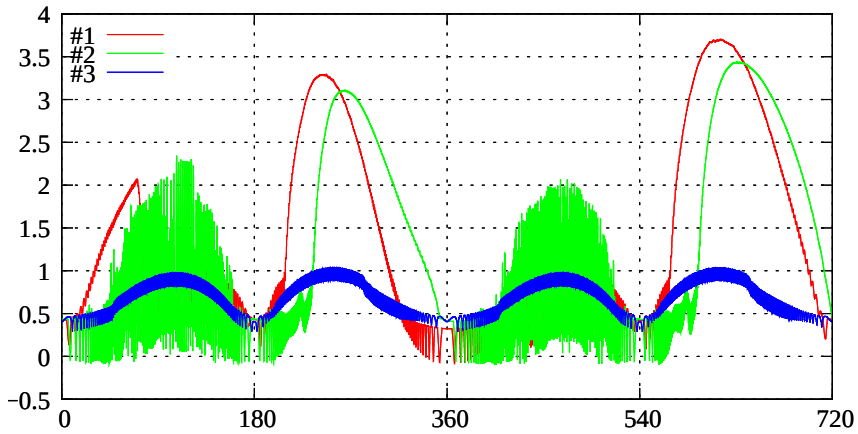

Figure 16: Radial position of the rings, for the transverse texture.

4 FINAL REMARKS

In this article we have reported, to our knowledge for the first time, numerical simulations of the piston-ring assembly along a full engine cycle with a conservative formulation, considering realistic applied loads on the rings and the actual crankshaft-connecting rod kinematics.

A detailed study was performed in the case of an untextured liner. It was shown that the oil ring only enters in solid contact with the liner near the top and bottom dead centers. The wiper ring, on the other hand, is in solid contact along the suction and power strokes, during which its friction is governed by the solid-solid friction coefficient. The compression ring exhibits a more interesting behavior. During the compression and blow strokes it is in the hydrodynamic regime, with low frictional dissipation. During the suction and power strokes, however, after the oil accumulated on top of the wiper ring has been depleted it enters into starvation, with high frictional dissipation. The overall non-dimensional friction power equals 0.1105, decomposed as 0.0498 for Ring 1, 0.0342 for Ring 2 and 0.0265 for Ring 3. Also, 0.038 corresponds to hydrodynamic losses and 0.072 to solid-contact losses.

Another study was carried out for a transversely textured liner. In this case it was observed that the wiper ring enters into a chaotic, unstable behavior that ends up maintaining the ring at a quite large average distance from the liner. This makes the wiper to not act according

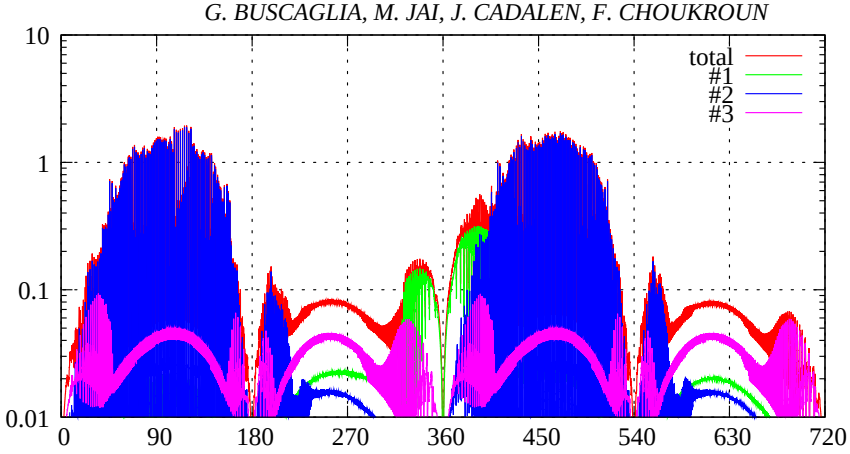

Figure 17: Friction power loss, for the transverse texture.

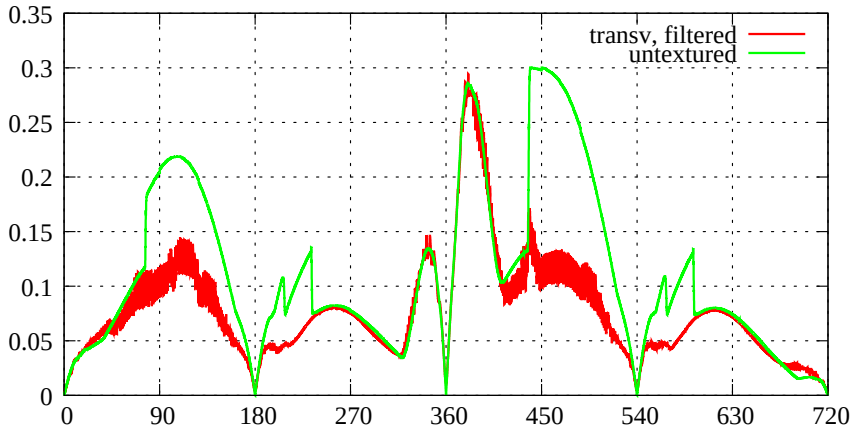

Figure 18: Filtered friction power loss, for the transverse texture, as compared to the untextured case.

to its function and a much larger flow of oil reaches the compression ring in the suction and power strokes. The consequence is similar to simply removing the wiper ring, with the obvious reduction in friction losses but no practical interest. This instability is probably stronger in our simulations than it would be in a real engine, since to save computing time we took the rings' masses with values multiplied by a factor of ten.

Finally, a study with a cross-striated liner at an angle of 60 degrees was carried out. The average friction losses turned out to be 0.1218, with 0.0415 for Ring 1, 0.0322 for Ring 2 and 0.0482 for Ring 3. Notice that the friction of the oil ring increases significantly, showing that the texture increases the friction in the hydrodynamic regime. At the same time, notice that the friction of the compression ring is significantly reduced by the texture. This is just a consequence of more oil passing between the wiper and the liner, which inhibits the starvation of the compression ring during the downward strokes. The oil consumption, on the other hand, would increase accordingly.

We end this report with a word of caution on the validity of the numerical model. It should be kept in mind that the model does not transport the oil content with the correct velocity in the region between rings. As a consequence, the oil film spontaneously spreads after the passage of each ring. In other words, the oil does not remain inside the striations, it spreads so as to make the oil thickness constant, which is unrealistic. This spurious spreading may overestimate the

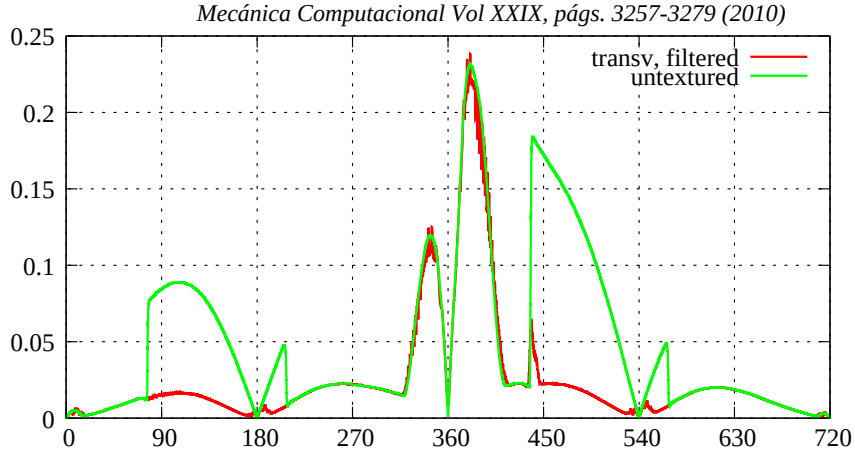

Figure 19: Filtered friction power loss at the compression ring, for the transverse texture, as compared to the untextured case.

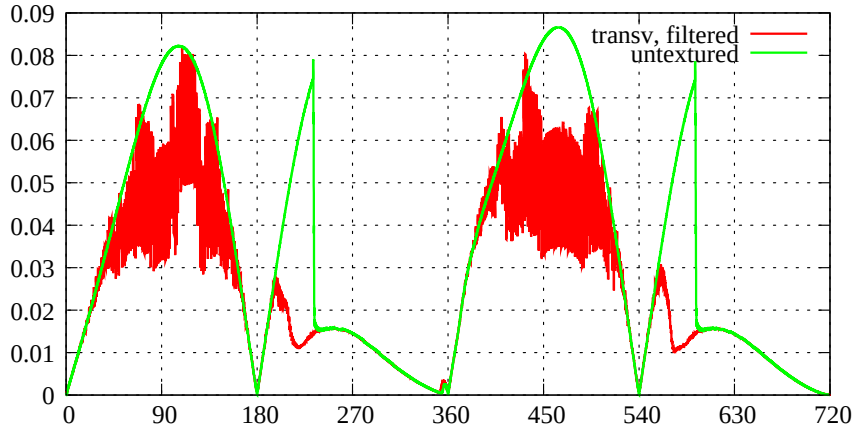

Figure 20: Filtered friction power loss at the wiper ring, for the transverse texture, as compared to the untextured case.

capabilities of the cross-striated texture in inhibiting starvation of the compression ring. Also, notice that the change in the shape of the rings caused by wear (particularly severe for the wiper ring) has not been accounted for, and that the pressure to the right of the compression ring has not been made to coincide with the cylinder pressure. These refinements require more accurate experimental data and a modification of the algorithm that will be addressed in future work.

ACKNOWLEDGMENTS: This work was carried out while GCB was visiting the INSA de Lyon. Partial support from CNPq and FAPESP is gratefully acknowledged.

REFERENCES

Ausas R., Jai M., and Buscaglia G. A mass-conserving algorithm for dynamical lubrication problems with cavitation. *ASME Journal of Tribology*, 131:031702 (7 pages), 2009a.

Ausas R., Ragot P., Leiva J., Jai M., Bayada G., and Buscaglia G. The impact of the cavitation model in the analysis of micro-textured lubricated journal bearings. *ASME Journal of Tribology*, 129:868–875, 2009b.

Bayada G. and Chambat M. The transition between the Stokes equations and the Reynolds equation: A mathematical proof. *Applied Mathematics & Optimization*, 14(1):73–93, 1986.

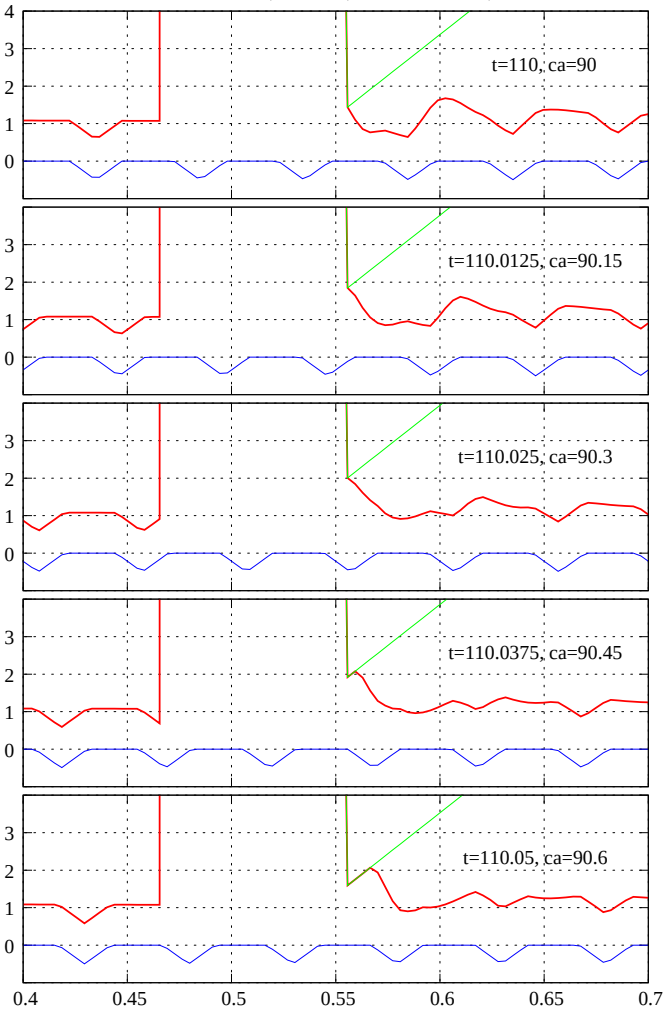

Figure 21: Oil thickness profiles near crank angle of 90 degrees at the wiper ring. Transverse texture.

Bayada G., Chambat M., and El Alaoui M. Variational formulations and finite element algorithms for cavitation problems. *ASME Journal of Tribology*, 112:398–403, 1990.

Dobrica M. and Fillon M. About the validity of reynolds equation and inertia effects in textured sliders on infinite width. *Proc. IMechE*, 223:69–78, 2008.

Elrod H.G. and Adams M. A computer program for cavitation. Technical report 190. *1st LEEDS LYON Symposium on Cavitation and Related Phenomena in Lubrication, I.M.E.*, 103:354, 1974.

Greenwood J. and Williamson J. Contact of nominally flat surfaces. *Proceedings of the Royal Society of London. Series A, Mathematical and Physical Sciences*, 295:300–319, 1966.

Panayi A. and Schock H. Approximation of the integral of the asperity height distribution for the greenwoodâĂŞtripp asperity contact model. *Proceedings of the Institution of Mechanical Engineers, Part J: Journal of Engineering Tribology*, 222:165–169, 2008.

Priest M. *The wear and lubrication of piston rings*. Ph.D. thesis, University of Leeds, 1996.

Priest M. Factors influencing boundary friction and wear of piston rings. *Tribology series*, 38:409–416, 2000.

Priest M. and Dowson D.and Taylor C.M. Predictive wear modelling of lubricated piston rings in a diesel engine. *Wear*, 231(1):89–101, 1999.

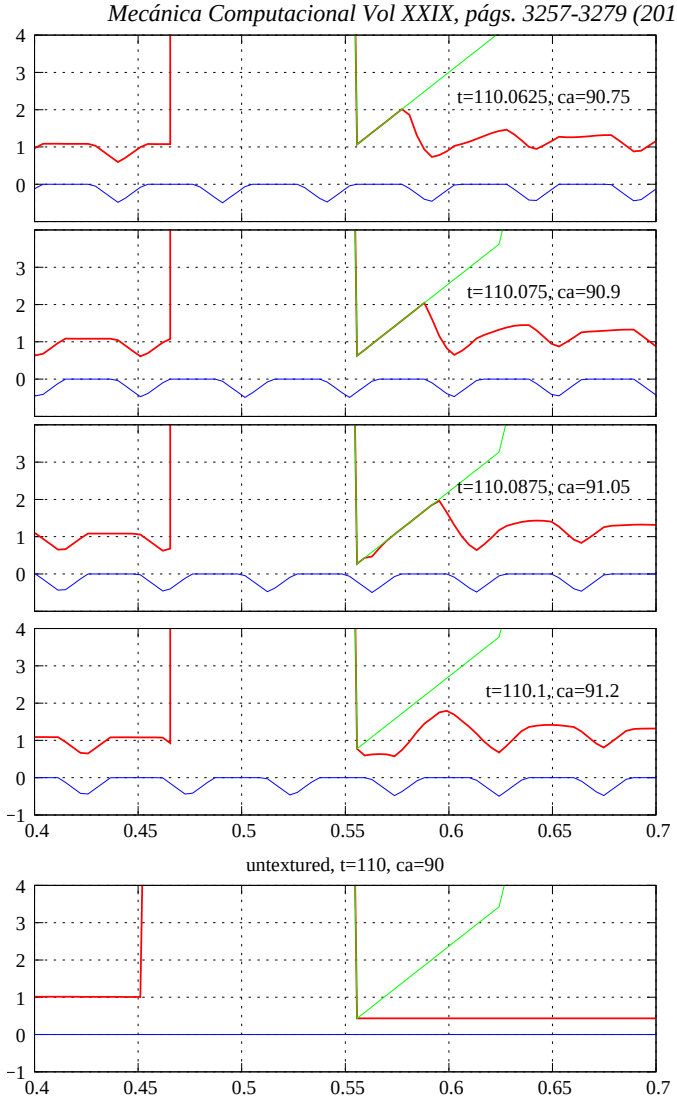

Figure 22: Oil thickness profiles near crank angle of 90 degrees at the wiper ring. Transverse texture. Compare to the bottom figure, corresponding to the untextured liner.

Priest M. and Dowson D.and Taylor C.M. Theoretical modelling of cavitation in piston ring lubrication. *Proc. Instn. Mech. Engrs*, 214(1):435–447, 2000.

Qiu Y. and Khonsari M. On the prediction of cavitation in dimples using a mass-conservative algorithm. *ASME, J. of Trib.*, 131:041702–1, 2009.

Uehara Y., Wakuda M., Yamauchi Y., Kanzaki S., and Sakaguchi S. Tribological properties of dimpled silicon nitride under oil lubrication. *J. Eur. Ceramic Society*, 24:369–373, 2004.

Wakuda M., Yamauchi Y., Kanzaki S., and Ysuda Y. Effect of surface texturing on friction reduction between ceramic and steel materials under lubricated sliding contact. *Wear*, 254:356–363, 2003.

Yagi K., Takedomi W., Tanaka H., and Sugimura J. Improvement of lubrication performance by micro pit surfaces. *Tribology Online*, 3:285–288, 2008.

Yu H., Wang X., and Zhou F. Geometric shape effects of surface texture on the generation of hydrodynamic pressure between conformal contacting surfaces. *Tribology Letters*, 37:123–130, 2010.

Zienkiewicz O. and Taylor R. *The finite element method*, volume II. McGraw Hill, 1991.

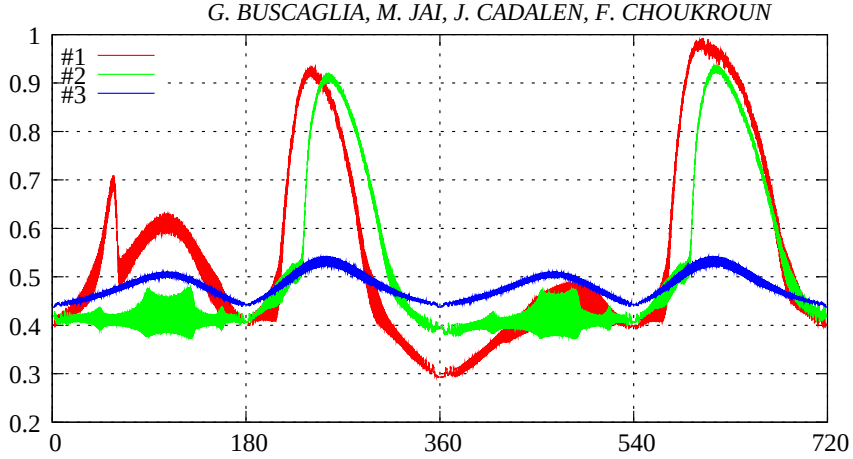

Figure 23: Radial position of the rings, for the cross-striated liner.

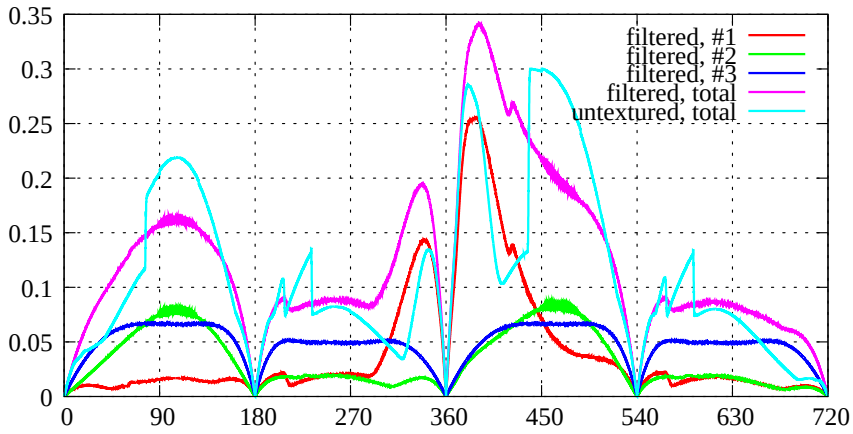

Figure 24: Filtered friction power along the cycle, for the cross-striated liner.

Zum Gahr K., Mathieu M., and Brylka B. Friction control by surface engineering of ceramic sliding pairs in water. *Wear*, 263:920–929, 2007.

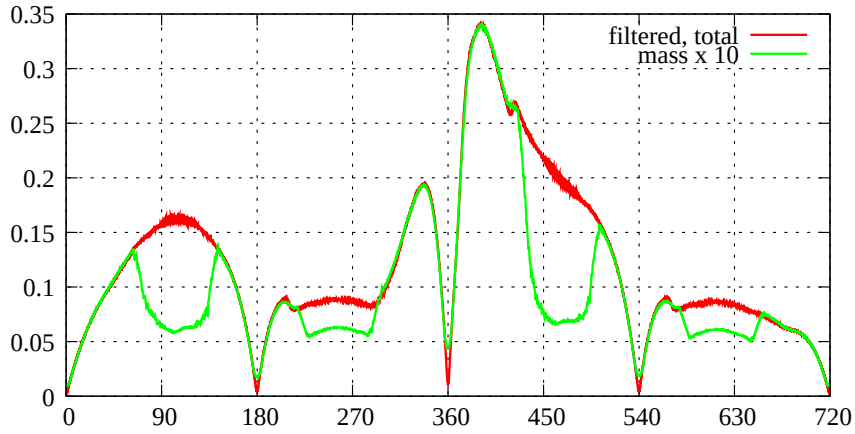

Figure 25: Filtered friction power along the cycle, for the cross-striated liner. Effect of multiplying by 10 the masses of the rings.

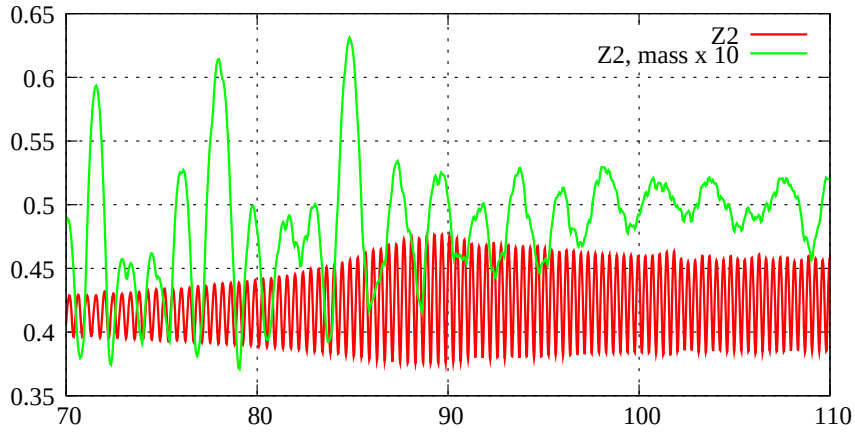

Figure 26: Minimum distance between Ring 2 (wiper) and the liner, for the cross-striated case. Effect of multiplying by 10 the masses of the rings.